

Magnetic anisotropy in ferromagnetic CrI₃

Lebing Chen¹, Jae-Ho Chung^{2,*}, Tong Chen,¹ Chunruo Duan,¹ Astrid Schneidewind³, Igor Radelytskyi,³ David J. Voneshen,⁴ Russell A. Ewings⁵,⁴ Matthew B. Stone⁵, Alexander I. Kolesnikov⁵, Barry Winn,⁵ Songxue Chi,⁵ R. A. Mole,⁶ D. H. Yu,⁶ Bin Gao¹, and Pengcheng Dai^{1,5,†}

¹Department of Physics and Astronomy, Rice University, Houston, Texas 77005, USA

²Department of Physics, Korea University, Seoul 02841, Korea

³Forschungszentrum Jülich GmbH, Jülich Centre for Neutron Science (JCNS) at Heinz Maier-Leibnitz Zentrum (MLZ), Lichtenbergstrasse 1, 85748 Garching, Germany

⁴ISIS Pulsed Neutron and Muon Source, STFC Rutherford Appleton Laboratory, Harwell Campus, Didcot, Oxon, OX11 0QX, United Kingdom

⁵Neutron Scattering Division, Oak Ridge National Laboratory, Oak Ridge, Tennessee 37831, USA

⁶Australian Nuclear Science and Technology Organisation, Locked bag 2001, Kirrawee DC, New South Wales 2232, Australia



(Received 27 August 2019; revised manuscript received 7 December 2019; accepted 23 March 2020;
published 15 April 2020)

We use neutron scattering to show that ferromagnetic (FM) phase transition in the two-dimensional (2D) honeycomb lattice CrI₃ is a weakly first order transition and controlled by spin-orbit coupling (SOC) induced magnetic anisotropy, instead of magnetic exchange coupling as in a conventional ferromagnet. With increasing temperature, the magnitude of magnetic anisotropy, seen as a spin gap at the Brillouin zone center, decreases in a power law fashion and vanishes at T_C, while the in-plane and c-axis spin-wave stiffnesses associated with magnetic exchange couplings remain robust at T_C. We also compare parameter regimes where spin waves in CrI₃ can be described by a Heisenberg Hamiltonian with Dzyaloshinskii-Moriya interaction or a Heisenberg-Kitaev Hamiltonian. These results suggest that the SOC induced magnetic anisotropy plays a dominant role in stabilizing the FM order in single layer 2D van der Waals ferromagnets.

DOI: 10.1103/PhysRevB.101.134418

I. INTRODUCTION

Understanding the microscopic origin of two-dimensional (2D) ferromagnetic (FM) order and spin dynamics in van der Waals materials is important for their potential magnet-based applications [1]. In a conventional three-dimensional (3D) cubic spin-rotation invariant (spin isotropic) ferromagnet, the Curie temperature T_C associated with the second order FM phase transition is determined by the short-range magnetic exchange coupling J [2]. In the low wave-vector (q → 0) limit, spin-wave energies E follow the well-known quadratic dispersion relation E = Δ(T) + D(T)q², where D(T) [D(T → 0) ∝ J] is the spin-wave stiffness and Δ(T) is a vanishingly small dipolar gap [2]. The quadratic dispersion form, however, is general for any ferromagnet and not limited to the Heisenberg model [2]. According to the hydrodynamic and mode-mode coupling theories, temperature dependence of the spin-wave stiffness in a second order FM phase transition must vanish at T_C via D(T) ∝ (1 - T/T_C)^{ν+β}, where ν and β are critical exponents of the magnetic phase transition [3,4]. For a typical 3D Heisenberg ferromagnet, we expect (ν + β) ≈ 0.34 compared with the measured values for iron (0.36 ± 0.03), cobalt (0.39 ± 0.05), and nickel (0.39 ± 0.04) [4]. When the dimensionality of the magnetic system is reduced from 3D to 2D, Mermin and Wagner showed the absence

of long-range FM or antiferromagnetic (AF) order at finite temperature in spin-rotational invariant systems with short-range magnetic interactions [5]. Although the long-range FM order in 2D systems at finite temperature can be brought about by breaking the spin-rotational invariance [6], the ordering temperature is again expected to be determined by J, resulting in D(T) → 0 at T_C [1,4,6,7]. Therefore, the discovery of robust FM order in van der Waals monolayers of CrI₃ [8] and Cr₂Ge₂Te₆ [9] raised an important question concerning the magnetic interactions that break the spin-rotational invariance and stabilize the finite temperature 2D FM order.

In principle, spin rotational invariance of a 3D magnetic system can be broken via dipolar interactions [10], single-ion (magnetocrystalline) anisotropy [11], and/or anisotropic magnetic exchange interactions [12,13]. For layered honeycomb lattice ferromagnet such as CrI₃ [Figs. 1(a) and 1(b)] [14], another possible mechanism that can break spin rotational invariance is the off-diagonal term Γ in the Heisenberg-Kitaev (J-K-Γ) Hamiltonian [Fig. 1(c)] [15–23]. For bulk CrI₃, which orders ferromagnetically below T_C ≈ 61 K, the FM order is believed to be a second order phase transition [14]. In addition, there is a strong magnetic anisotropy revealed as a large difference in the saturation magnetic field for field parallel to the c-axis direction (H_c^S) and in the ab plane (H_{ab}^S and H_{ab}^S ≈ H_c^S ≈ 3 T) [14,24]. By comparing the temperature dependence of the magnetic anisotropy of CrI₃ with those of CrBr₃, it was concluded that the magnetic anisotropy in CrI₃ arises from a dominant uniaxial or single-ion anisotropy [24], which comes mostly from the

*jaehc@korea.ac.kr
†pdai@rice.edu

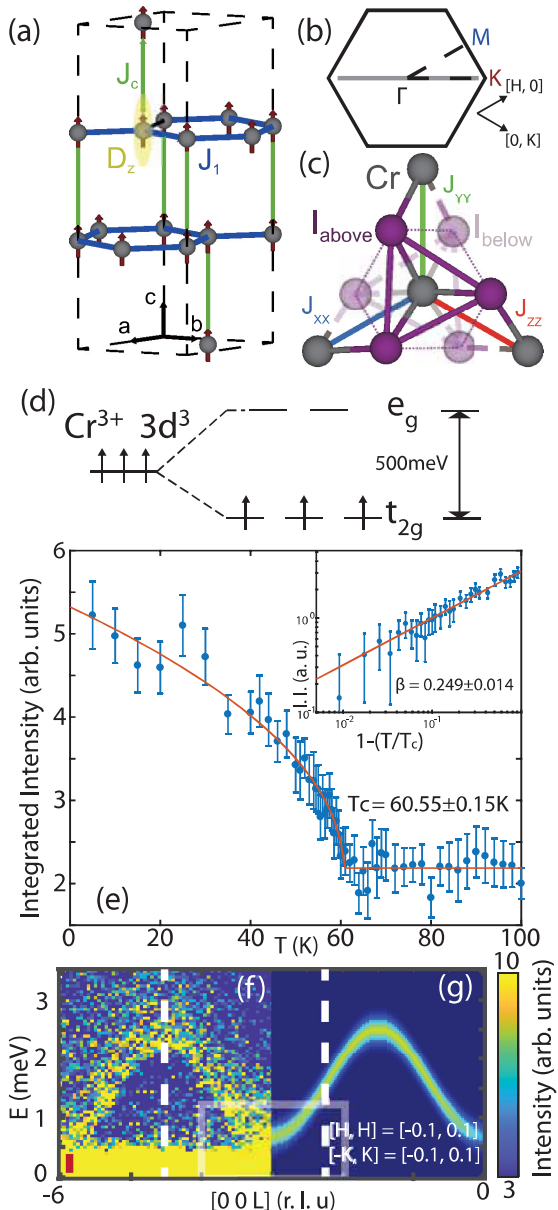


FIG. 1. (a) Crystal structure of CrI_3 , where the nearest neighbor magnetic exchange couplings within the Cr plane and along the c axis are J_1 and J_c , respectively. The D_z is the single-ion anisotropy. (b) Reciprocal space within the $[H, K]$ plane, where Γ , K , M points are specified. The gray line indicates the Q direction for constant-energy scans. (c) Real space picture of CrI_3 , where the nearest-neighbor I atoms form an octahedral environment with 3 I above (dark purple) and 3 I below (light purple) the Cr layer. The Cr-I-Cr path forms an angle close to 90 degrees [12,13]. The Kitaev interactions between Cr^3 atoms are marked as J_{xx} , J_{yy} , and J_{zz} [18]. (d) The CEF level of the I octahedra splits the d levels in the e_g and t_{2g} manifolds. (e) Magnetic order parameter at the $(1, 1, 0)$ position. The inset is a log-log plot of the integrated magnetic peak intensity. Both red lines are power law fits with the same critical exponent $\beta = 0.249 \pm 0.014$. (f) Spin-wave dispersion along the $[0, 0, L]$ direction at $T = 3$ K obtained with $E_i = 5.2$ meV. (g) The Heisenberg model fit of the c -axis dispersion. The dashed lines in (f) and (g) indicate const- Q scans in Figs. 2(c) and 2(d). Red bars in (f) and Figs. 2(a), 2(c), 2(d), 2(e), 3(a), and 4(a) are instrumental energy resolution [23].

interplay between spin-orbit coupling (SOC) of the Cr magnetic ion with the crystal electric field (CEF) levels induced by its surrounding I atoms arranged in edge sharing octahedra [Figs. 1(c) and 1(d)]. Since dipolar interactions typically are very small and favor in-plane anisotropy [10], their effects on spin rotation anisotropy are negligible and can be safely ignored [12,13]. On the other hand, single-ion anisotropy in CrI_3 has been estimated to be way below 1 meV because of the quenched orbital moment of Cr^3 and the large energy separation (≈ 500 meV) of the CEF excited states of the Cr^3 ion [Figs. 1(c) and 1(d)] [12,13]. Finally, spin rotational invariance of a magnetic system such as CrI_3 can also be broken because of the magnetic anisotropy arising from the Cr 3d-I p-Cr 3d superexchange hopping in the near 90° bonding angle networks [Fig. 1(c)] [12,13].

If magnetism in 3D CrI_3 also breaks the spin rotational invariance and becomes anisotropic in real space, it should reveal itself as a gap in spin-wave dispersion at the Γ point in Fig. 1(b) with $\Delta > 0$, in contrast to the $\Delta \approx 0$ seen in typical isotropic ferromagnets [25,26]. In principle, one can detect such a gap by FM resonance [27], Raman scattering [28], or inelastic neutron scattering (INS) [25,26]. Using FM resonance [29], a spin gap of ~ 0.3 meV was estimated at the Γ point below T_C [18]. On the other hand, polarized micro-Raman spectroscopy experiments on CrI_3 found evidence for two sets of zero wave-vector spin waves at 9.4 meV and 15.5 meV [30]. Since CrI_3 has two magnetic ions per unit cell, giving rise to only one acoustic and one optical spin-wave branches [18,30,31], the Raman spectroscopy results suggest a spin gap of 9.4 meV at the Γ point [30]. Finally, INS experiments on single crystals of CrI_3 revealed a ~ 4 meV spin gap at the Dirac (K) points but found no evidence of a spin gap above ~ 1 meV at the Γ point [31]. While FM resonance [18] and INS [31] results are clearly in contrast to those of Raman spectroscopy [30], the actual value of the anisotropy gap is still undetermined. To conclusively determine the size of the spin gap and its temperature dependence, and test if spin dynamics in CrI_3 are consistent with a Heisenberg ferromagnet [4], INS experiments are necessary.

II. RESULTS

In this paper, we report INS studies of spin waves in CrI_3 . We have also carried out elastic and quasielastic neutron scattering experiments to study the nature of the FM phase transition in CrI_3 . In addition to confirming a spin gap of $\Delta = 0.37 \pm 0.02$ meV at $T = 3$ K and the Γ point, we trace the temperature dependence of $\Delta(T)$ and $D(T)$ across T_C . While spin-wave stiffness within the CrI_3 plane $D_{\text{HH}}(T)$ is considerably larger than that of the stiffness along the c -axis $D_L(T)$, they both do not vanish at T_C , contrary to the expectation of a 3D [3,4] or 2D [1,6,7] Heisenberg ferromagnet with a second order FM phase transition. On the other hand, the anisotropy gap $\Delta(T)$ has an order-parameter-like temperature dependence and vanishes at T_C . These results, together with the lack of magnetic critical scattering around T_C and finite spin-spin correlation length in the low-temperature FM ordered state, suggest that the FM phase transition in CrI_3 is weakly first order instead of a second order phase transition. We thus conclude that the breaking of the spin-rotation

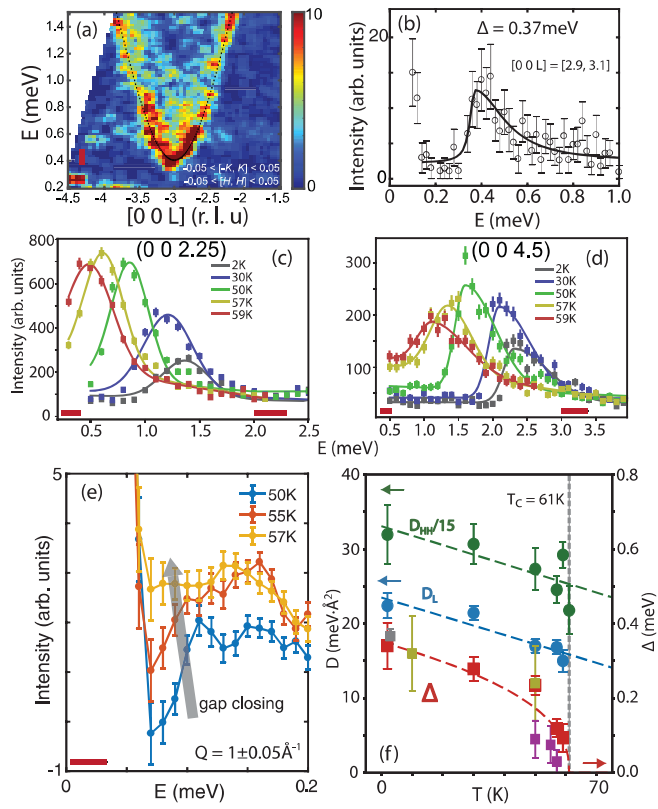


FIG. 2. (a) Images of spin waves near the Γ point. (b) An energy cut of the data at $Q = (0, 0, \hat{a} 3)$. (c) Constant- Q scans for $Q = (0, 0, 2.25)$. (d) Similar scans at $Q = (0, 0, 4.5)$. (e) Temperature dependence of the spin gap around the Γ point [23]. (f) Temperature dependence of the $D_{HH}(T)$ (green dots), $D_L(T)$ (blue dots), and $\Delta(T)$ (gray (LET), red (PANDA), yellow and purple (both Pelican) colored squares), where the dashed line is a fit to the power law equation. The green and blue dashed lines are guides to the eye.

invariance via large SOC is ultimately responsible for stabilizing the FM order in 3D and monolayer CrI₃, and other monolayer materials [1,32–35].

We carried out some of the measurements using the LET neutron time-of-flight chopper spectrometer at Rutherford-Appleton Laboratory, Didcot, UK [36]. The experiments were carried out with multi- E_i (incident beam energy) mode (E_i = 25 meV, 5.37 meV [Fig. 1(f)] and 2.27 meV [Figs. 2(a) and 2(b)]) with single crystals of CrI₃ fixed at $T = 3$ K. A Horace scan was done on co-aligned 0.42 g single crystals of CrI₃ with the sample in the [H, H, L] scattering plane [37]. Using a honeycomb structure with in-plane Cr-Cr distance of $a - b \approx 3.96$ Å and c-axis layer spacing of $c = 19.81$ Å in the low temperature rhombohedral structure [Fig. 1(a)] [38], the momentum transfer $Q = Ha^* Kb^* Lc^*$ is denoted as $Q = (H, K, L)$ in reciprocal lattice units (r.l.u.) [Fig. 1(b)] [31].

We have also carried out INS experiments on the cold neutron triple-axis spectrometer PANDA at Heinz Maier-Leibnitz Zentrum, Garching, Germany [Figs. 2(c) and 2(d)] [39]. The experiments were carried out with a fixed final neutron energy of $E_f = 3.78$ meV. Constant- E scans were performed along the [H, H, 3] direction at temperatures of 2 K, 30 K, 50 K, 57 K, 59 K, 61 K, 63 K, 68 K, 73 K, 78 K, 84 K, and 250 K.

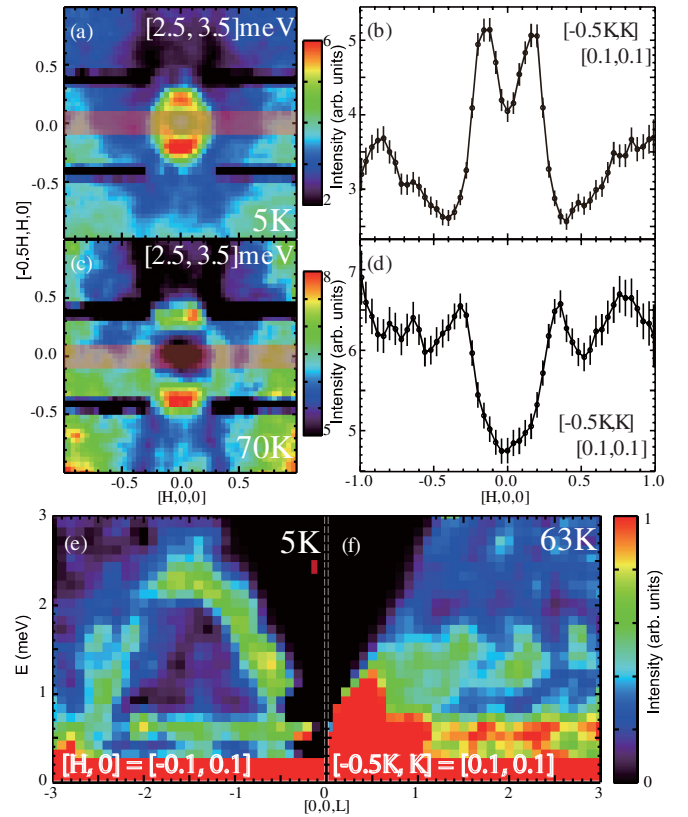


FIG. 3. (a) Low energy ($E = 3 - 0.5$ meV) spin waves of CrI₃ in the [H, K] plane at $T = 5$ K. (b) A cut along the [H, 0] direction. (c) The same scan as (a) but at $T = 1.14T_C$. (d) The same cut as (b) at $T = 1.14T_C$. The red boxes in (a) and (c) show the integration range in (b) and (d), respectively, with L integrated from [$\hat{a} 5, 5$]. (e) Spin wave dispersion along the c axis at $T = 5$ K. (f) Identical scan at $T = 1.03T_C$. The data was collected using $E_i = 8$ meV [23].

Constant- Q scans are performed at $Q_{2.25} = (0, 0, 2.25)$ and $Q_{4.5} = (0, 0, 4.5)$ with sample temperatures of 2 K, 30 K, 50 K, 57 K, and 59 K [Figs. 2(c) and 2(d)]. The sample mass is 0.84 g of co-aligned single crystals of CrI₃. To get the anisotropy gap Δ and D_L along the c axis, which is related to the spin-wave bandwidth E_{band} along the [0, 0, L] direction, we used a sinusoidal fit to estimate the values of D_L and Δ in Fig. 2(f).

To accurately determine the temperature dependence of the gap $\Delta(T)$ at the Γ point around T_C , we carried out INS measurements using the PELICAN time-of-flight neutron spectrometer at ANSTO, Australia [Figs. 2(e) and 2(f)] [40]. These experiments were performed on 14 g powder samples of CrI₃ at 10 K, 50 K, 55 K, and 57 K. Two incident energies, $E_i = 3.7$ and 2.3 meV, were used to probe the anisotropy gap $\Delta(T)$ located at $Q = (0, 0, 3)$ (corresponding to $q_{gap} = 0.96$ Å⁻¹). The anisotropy gap value $\Delta(T)$ is extracted by subtracting the integrated intensity in the range $(q_{gap} \pm 0.05) - (q_{gap} \pm 0.05)$ Å⁻¹ by an average of the intensity in the range $(q_{gap} \pm 0.35) - (q_{gap} \pm 0.25)$ Å⁻¹ and $(q_{gap} \pm 0.25) - (q_{gap} \pm 0.35)$ Å⁻¹ [23].

Our experiments on neutron time-of-flight chopper spectrometer SEQUOIA at spallation neutron source, Oak Ridge National Laboratory (ORNL), Oak Ridge, Tennessee [41], were carried out with $E_i = 25$ meV [Figs. 3(a)–3(d)] and

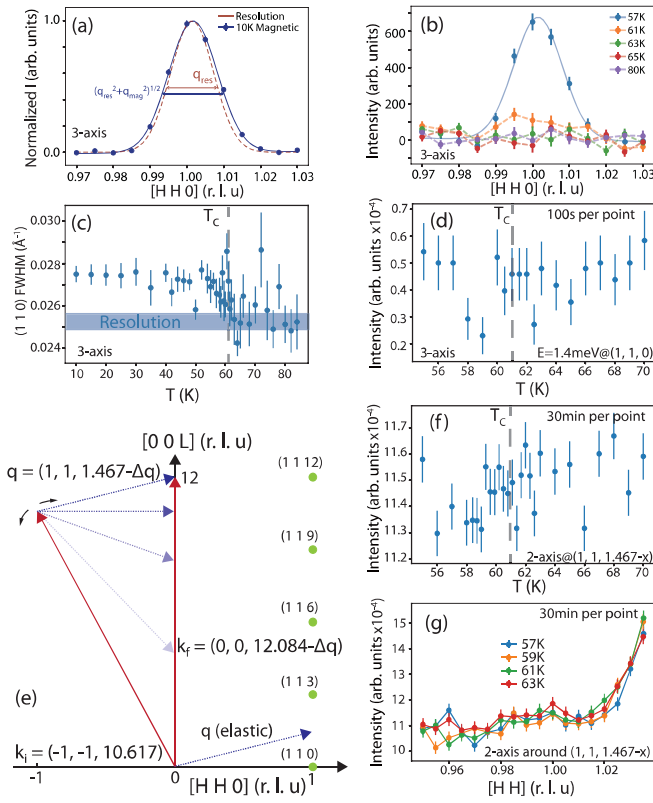


FIG. 4. (a) Wave vector dependence of the magnetic Bragg peak (1, 1, 0) along the [H, H, 0] direction obtained by subtracting the nuclear Bragg peak above T_c from the same scan at 10 K. The dashed line is the instrument resolution limited nuclear Bragg peak above T_c (80 K to 84 K). The data was collected on HB-3 with collimation of 48'-40'-40'-120' and final neutron energy of $E_f = 14.7$ meV. The blue line is a fit to Gaussian on a flat background, giving spin-spin correlation length of 220 ± 4 Å. (b) Temperature dependence of the magnetic scattering around the (1, 1, 0) position across T_c , where the high temperature nuclear Bragg peak is subtracted. (c) Temperature dependence of the full width at half maximum (FWHM) of the (1, 1, 0) peak across T_c . Above T_c , the FWHM shows instrumental resolution limited nuclear Bragg peak width. (d) Temperature dependence of the inelastic scattering at $E = 1.4$ meV and (1, 1, 0). (e) Schematics of the two-axis mode scan with neutron final wave vector k_f . The incident neutron energy E_i is fixed at 30.5 meV. The scattering intensity shown in (f) and (g) is integrated over all possible k_f . (f) Temperature dependence of the scattering at in-plane wave vector (1, 1, 0). (g) [H, H, 0] scans across the in-plane wave vector (1, 1, 0) around T_c using two-axis mode. The intensity obtained in (f) and (g) is an integration over all possible values of Δq in (e).

8 meV [Figs. 3(e) and 3(f)] at temperatures 5 K, 52 K, 63 K, and 70 K [23]. Horace scans are done on co-aligned 0.2 g single crystals of CrI₃ with the sample in the [H, 0, L] scattering plane. The 0.6 meV flat mode in Figs. 3(e) and 3(f) is an instrumental artifact.

The magnetic critical scattering is measured on the HB-3 thermal neutron triple-axis spectrometer at High-Flux Isotope Reactor, ORNL [Figs. 4(a)–4(g)]. The monochromator, analyzer, and filter are pyrolytic graphite (PG). For triple-axis measurements, final neutron energy of $E_f = 14.7$ meV was

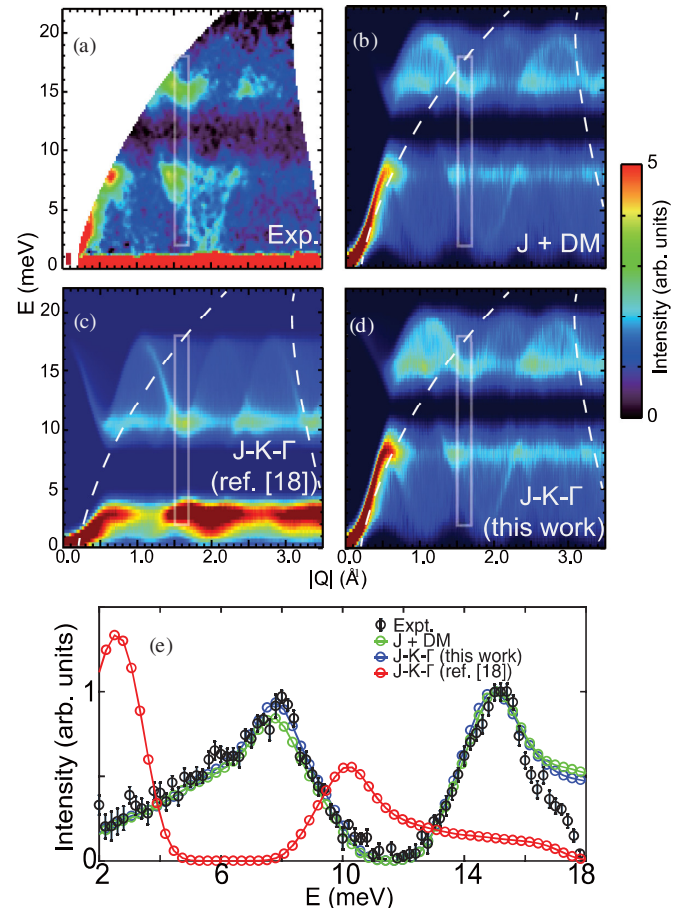


FIG. 5. (a) INS data of the CrI₃ powder at $T = 5$ K using $E_i = 25$ meV. (b)–(d) Powder-averaged spin-wave spectra calculated using the Heisenberg-DM [31], J-K-Γ Hamiltonian using parameters of Ref. [18], and new parameters ($J_1 = 0.17 \pm 0.05$ meV, $J_2 = 0.21 \pm 0.04$ meV, $K = 5.6 \pm 0.2$ meV), respectively. The dashed lines mark the limits of the data in (a). (e) The black, green, red, and blue points/lines are the experimental data, Heisenberg-DM, J-K-Γ Hamiltonian calculations with parameters of [18], and the new parameters mentioned above, respectively. The scan directions are marked as solid boxes in (a)–(d).

used and a PG filter was placed after the sample. For two-axis measurements, a PG filter was placed before the sample to reduce $\lambda/2$ and incident neutron energy was set at $E_i = 30.5$ meV. A single piece of CrI₃ single crystal (13 mg) with mosaic 1 degree was used in the experiment. The HYSPEC experiments [42] were performed on 6 g powder samples at 3 K [Fig. 5(a)]. A Horace scan is performed to eliminate the anisotropy inside the powder sample.

In an ionic picture, Cr³⁺ in CrI₃ has an electronic configuration $3s^0 3d^3$ and is surrounded by 6 I atoms in an octahedral environment [Fig. 1(c)]. The d levels of Cr³⁺ split into a higher energy e_g doublet and a lower energy t_{2g} triplet separated by ~ 500 meV [Fig. 1(d)] [12]. With the first Hund rule, three electrons in Cr³⁺ occupy the t_{2g} manifold in the S = 3/2 state with quenched orbital moment $\langle \vec{L} \rangle \simeq 0$ [Fig. 1(d)] [12,13]. Figure 1(e) shows temperature dependence of the (1, 1, 0) Bragg peak intensity, confirming

the FM transition at $T_C = 60.5 \pm 0.2$ K. The solid line in the figure is a fit to the magnetic order parameter by $I = I_0(1 - T/T_C)^{2\beta}$ [4]. Within the temperature range probed, we find $\beta = 0.25 \pm 0.01$ [inset in Fig. 1(e)]. This value is in between the critical exponents of 2D and 3D Ising ferromagnets [4,43], thus suggesting finite interplanar (c-axis) magnetic exchange coupling J_c in CrI₃. This is consistent with the spin-wave dispersion along the c axis at $T \approx 3$ K [Fig. 1(f)]. Figure 1(g) shows a fit to the spin-wave dispersion using a Heisenberg Hamiltonian [31].

Figure 2(a) shows spin waves near the Γ point, revealing an anisotropy gap of $\Delta = 0.37 \pm 0.02$ meV at $T = 3$ K. An energy cut at the spin-wave minimum indicates steplike intensity gain around 0.37 meV [Fig. 2(b)]. While the magnitude of Δ is smaller by a factor of two compared with estimation from previous measurements [31], it is consistent with the estimation from the FM resonance [18,29] and larger than in its isostructural compound CrBr₃ ($\Delta < 0.1$ meV) [44] and CrSiTe₃ ($\Delta \approx 0.075$ meV) [45], suggesting considerably stronger SOC in CrI₃.

To determine the temperature dependence of the magnetic exchange couplings within the CrI₃ plane and along the c axis, we measured spin-wave dispersions around the Γ point along the intraplanar [H, H, 3] [23] and interplanar [0, 0, L] directions. Figures 2(c) and 2(d) are the constant-Q scans to probe the temperature dependence of interplanar modes for temperatures up to $T = 59$ K ($= 0.97T_C$). Since the full interplanar spin-wave bandwidth could be observed [Fig. 1(f)], we performed variable-energy scans at $Q = (0, 0, 2.25)$ [Fig. 2(c)] and $(0, 0, 4.5)$ [Fig. 2(d)]. The zone boundary spin-wave energy at $T = 0.97T_C$ is reduced by $\sim 50\%$ [Fig. 2(d)], suggesting significant interplanar exchanges approaching the FM transition. Assuming that the interplanar dispersion follows the simple sinusoidal dependence on L [Fig. 1(f)], we can estimate the spin wave stiffness along the c-axis $D_L(T) \equiv a_L(T)(c/6)^2$ in units of meV Å² by fitting the data with $E = a_L(T)[\sin(\frac{\pi}{3}L)]^2 - \Delta(T)$. Figure 2(e) shows temperature dependence of the spin gap around the Γ point ($Q = 0.96 \pm 0.05$ Å⁻¹) approaching T_C [23]. Figure 2(f) summarizes temperature dependence of the in-plane [$D_{HH}(T)$] [23] and c-axis [$D_L(T)$] spin wave stiffnesses, revealing that the intraplanar and interplanar exchange couplings are almost fully active up to T_C in spite of the vanishing magnetization at T_C in Fig. 1(e). In contrast, $\Delta(T)$ obtained from the c-axis dispersion and direct measurements vanishes at T_C [see right axis in Fig. 2(f)] [23]. The dashed line shows a fit to the data using $\Delta(T) \propto (1 - T/T_C)^\alpha$, giving $\alpha = 0.35 \pm 0.14$.

At temperatures above T_C , spin excitations of CrI₃ become diffuse but still have signatures of the intraplanar modes. Figures 3(a) and 3(c) are images of the constant-energy slices ($E = 3.0 \pm 0.5$ meV) at $T = 5$ K and 70 K, respectively [23]. We see clear spin-wave-like rings in the [H, K] plane at both temperatures although the excitations are noticeably diffusive at $T = 70$ K ($= 1.14T_C$). Q-dependent cuts through data in Figs. 3(b) and 3(d) bear this out, showing some softening of the in-plane spin-wave energy on warming but is nonvanishing at T_C . Figures 3(e) and 3(f) show similar data along the c axis, where we see considerable yet incomplete ($\sim 50\%$) softening of the mode above T_C . Therefore, FM order in CrI₃ is not de-

terminated by the in-plane or c-axis magnetic exchange interactions as in a conventional 3D Heisenberg ferromagnet [4]. It is also different from the expectation of an ideal 2D Heisenberg ferromagnet [1,6,7].

To understand why $D(T)$ does not vanish at T_C in CrI₃ as required by the mode-mode coupling theory in a Heisenberg ferromagnet with second order phase transition [4], we consider the nature of the FM phase transition. In a second order FM phase transition, spin-spin correlation length and magnetic critical scattering should diverge at T_C [4]. Figure 4(a) compares the magnetic Bragg peak across the (1, 1, 0) reflection at 10 K with the instrumental resolution obtained by measuring the same nuclear Bragg peak above T_C . The magnetic Bragg peak width is clearly broader than the nuclear Bragg peak width, indicating that the spin-spin correlation length (~ 220 Å) is not resolution limited. Temperature dependence of the magnetic scattering around the (1, 1, 0) reflection in triple-axis mode reveals no peak above T_C [Fig. 4(b)], suggesting the lack of critical scattering around T_C . Figure 4(c) shows temperature dependence of the (1, 1, 0) peak width. At temperatures above T_C , the (1, 1, 0) peak width measures nuclear lattice correlation, which is instrumental resolution limited. On cooling below T_C , we see a clear broadening of the width that saturates below about 53 K, indicating that the in-plane spin-spin correlations in CrI₃ are short ranged even at 10 K and never reached the instrumental resolution (nuclear Bragg peak width) [Fig. 4(c)]. Temperature dependence of the inelastic scattering at $E = 1.4$ meV shows no anomaly at T_C , again suggesting no critical magnetic scattering.

While these results suggest that the FM phase transition in CrI₃ may be weakly first order instead of second order [14], a more stringent test is to measure the instantaneous spin correlations in CrI₃ across T_C [46]. In these two-axis neutron scattering measurements, the final neutron wave vector is aligned along the c-axis direction throughout the scan and all final neutron energies are integrated [Fig. 4(e)]. For a classical second order phase transition, we expect to observe critical spin fluctuations as a peak in the instantaneous spin correlations at the (1, 1, 0) position, and the peak intensity should diverge on approaching T_C from high temperature. However, the temperature dependence of the scattering at the (1, 1, 0) position reveals no anomaly across T_C [Fig. 4(f)]. The wave vector dependence of the scattering at various temperature across T_C also shows no obvious peak at the (1, 1, 0) position. If we assume that the FM phase transition in CrI₃ is indeed weakly first order instead of second order, we can understand the c-axis lattice distortion associated with the FM phase transition [14] and the peak in FM transition induced heat capacity anomaly [47]. The first order nature of the FM transition in CrI₃ provides a natural understanding for nonvanishing values of $D(T)$ at T_C , suggesting that FM order is not controlled by the magnetic exchange interaction in contrast to a Heisenberg Hamiltonian [4].

Another possible mechanism that can provide the spin anisotropy gap in honeycomb ferromagnets is the symmetric off-diagonal Γ term in the J-K- Γ Hamiltonian [18,22,23]. Whereas it also originates from the SOC, it is unlikely to be strong unless the diagonal K term is predominant. Figure 5(a) shows powder-averaged spin waves of CrI₃ at $T = 5$ K. To simulate the powder-averaged spin waves, we use

linear spin wave theory with the SpinW software as discussed in Ref. [48]. For the calculated powder spectra shown in Figs. 5(b)–5(d), the code chooses random orientation 1000 times to get an averaged intensity distribution.

The Heisenberg model Hamiltonian with DM interaction is

$$H = \sum_{i,j} [J_{ij} S_i \cdot S_j + A_{ij} S_i \cdot S_j] + \sum_j D_z (S_j^z)^2 \quad (1)$$

as in Ref. [31], where J_{ij} is the magnetic exchange coupling of the spin S_i and S_j , A_{ij} is the DM interaction between sites i and j , and D_z is the easy-axis anisotropy along the z (c) axis. Figure 5(b) shows our simulated spin waves with the intralayer term $J_1 \approx 2.13$ meV, $J_2 \approx 0.09$ meV, $J_3 \approx 0.10$ meV, interlayer term $J_c \approx 0.59$ meV, and anisotropy term $D_z \approx 0.20$ meV. For the choice of the DM term A_{ij} , we used 0.194 meV in the calculation in Fig. 5(b). The DM term in Ref. [31] ($D_z \approx 0.31$ meV) is overestimated due to the poor sample mosaic.

The Heisenberg-Kitaev (J-K- Γ) model Hamiltonian is

$$H = \sum_{(i,j) \in \lambda, \mu, \nu} [J_{ij} S_i \cdot S_j + K S_i^\nu S_j^\nu + \Gamma (S_i^\lambda S_j^\phi + S_i^\phi S_j^\lambda)], \quad (2)$$

where (λ, ϕ, ν) any permutation of (x, y, z) . For the simulation reproducing that of Ref. [18], we choose $J_1 \approx 0.212$ meV for the Heisenberg term, $K \approx 5.19$ meV for the Kitaev term, and $\Gamma \approx 0.0675$ meV for the symmetric off-diagonal anisotropy. We keep the interlayer exchange term J_c the same as in the Heisenberg-DM model in Figs. 5(c)–5(e).

As shown in Figs. 5(c) and 5(e), the model reproducing Ref. [18] is clearly not consistent with the powder neutron scattering data because the model parameters give incorrect energy of the gap. The simplest way to solve the problem is to introduce next neighbor magnetic exchange J_2 into the J-K- Γ Hamiltonian. To make optimal simulation using the J-K- Γ model, we fit the INS data in Ref. [31] with the J-K- Γ model, and the fitting result gives $J_1 \approx 0.17$ meV, $J_2 \approx 0.21$ meV, $K \approx 5.6$ meV, and $\Gamma \approx 0.075$ meV. Using these parameters, we get the simulation results in Fig. 5(d). These results suggest that the J-K- Γ model can have parameters regimes, similar to the Heisenberg-DM model in Ref. [31], that can describe the observed spin-wave spectra in CrI₃. The parameters in the new fit are similar to that in Ref. [18], except we must now introduce J_2 in order to shift the Dirac gap from 5–8 meV to 10–13 meV. Figure 5(e) compares experimental data with Heisenberg-DM, J-K- Γ Hamiltonian with different fitting parameters along the boxed directions in Figs. 5(a)–5(d), confirming that spin waves in CrI₃ can be described by the J-K- Γ Hamiltonian but with parameters different from those in Ref. [18].

III. DISCUSSION

The direct relation between the magnetic anisotropy and FM phase transition is revealed in the similar temperature dependence of the spin gap $\Delta(T)$ in Fig. 2(f) and magnetic order parameter in Fig. 1(e). The c -axis component of the ordered moment, S_z^z , is included in the anisotropic interaction term of the nearly-isotropic Heisenberg Hamiltonian $H \approx \sum_{i,j} J_{ij} S_i \cdot S_j + \sum_{(i,k)} A_{ik} S_i^z S_k^z$, where S_i is the spin on site

i . The A_{ik} in the second term accounts for the single-ion anisotropy or anisotropic exchange constant, with c being the easy axis, when the summation is over $i \neq k$ or $i = k$, respectively. If the anisotropic exchanges are limited to the nearest-neighbor bonds, the linear spin-wave energies calculated using $A_{i,k}$ ($\equiv A$) are equal to those using the single-ion anisotropy $A_{i,k}$ ($\approx 3A$). Therefore, the resulting spin-wave spectra exhibiting anisotropy gap will also be indistinguishable. Regardless of whether the spin gap is induced by single-ion or magnetic exchange anisotropy, the microscopic origin is the strong SOC induced by Cr-I interaction in CrI₃. Since the CrI₆ octahedra has little structural distortions below T_C [14], anisotropic Heisenberg exchange due to the SOC via Cr 3d-I p-Cr 3d superexchange path interaction is likely responsible for the FM order in CrI₃ [12,13].

IV. CONCLUSIONS

In conclusion, we used INS to show that the stiffness of the intraplanar and interplanar spin waves of CrI₃ has a finite value at T_C . While these results are contrary to the expectation of a 3D Heisenberg Hamiltonian with second order FM phase transition, they are consistent with our careful critical magnetic scattering measurements suggesting that the FM phase transition in CrI₃ is a weakly first order transition. Since the anisotropy gap is fully closed at T_C following similar temperature dependence as the order parameter, we conclude that the anisotropic SOC plays a decisive role in the FM phase transition in 3D CrI₃ and is responsible for stabilizing the FM order in monolayer CrI₃. We are not aware of a ferromagnet where the Curie temperature is controlled by SOC instead of the magnetic exchange coupling. Since spin waves in a ferromagnet are Goldstone modes, they are more unstable than spin waves in an antiferromagnet if there is no magnetic anisotropy. For example, it is well known that spin-wave-like excitations can appear above T_N in antiferromagnets, and temperature dependence of anisotropy gap follows the magnetic ordering parameter [49,50]. By judiciously adjusting the strength of SOC in 2D materials, one can control T_C of the system [1,32–35]. While monolayer CrI₃ orders ferromagnetically at $T_C \approx 45$ K [8], monolayer CrBr₃ can only order $T_C \approx 34$ K due to the reduced SOC [51], and long-range FM order will probably not survive in monolayer CrCl₃.

ACKNOWLEDGMENTS

We are grateful to R. J. Birgeneau and Andriy Nevidomskyy for helpful discussions. The INS and single crystal synthesis work at Rice was supported by the US NSF Grant No. DMR-1700081 and the Robert A. Welch Foundation Grant No. C-1839 (P.D.), respectively. The work of J.-H.C. was supported by the National Research Foundation of Korea (Grants No. NRF-2016R1D1A1B03934157 and No. NRF2017K1A3A7A09016303). A portion of this research used resources at the Spallation Neutron Source and the High Flux Isotope Reactor, a DOE Office of Science User

Facility operated by ORNL. Experiments at the ISIS Neutron and Muon Source were supported by a beam time allocation RB1820251 from the Science and Technology Facilities Council [52].

- [1] M. Gibertini, M. Koperski, A. F. Morpurgo, and K. S. Novoselov, *Nat. Nanotechnol.* **14**, 408 (2019).
- [2] S. Lovesey, *Theory of Thermal Neutron Scattering from Condensed Matter* (Clarendon, Oxford, 1984), Vol. 2.
- [3] J. Zhang, F. Ye, H. Sha, P. Dai, J. A. Fernandez-Baca, and E. W. Plummer, *J. Phys.: Condens. Matter* **19**, 315204 (2007).
- [4] M. Collins, *Magnetic Critical Scattering* (Clarendon, Oxford, 1989).
- [5] N. D. Mermin and H. Wagner, *Phys. Rev. Lett.* **17**, 1133 (1966).
- [6] M. T. Hutchings, J. Als-Nielsen, P. A. Lindgard, and P. J. Walker, *J. Phys. C: Solid State Phys.* **14**, 5327 (1981).
- [7] H. E. Stanley and T. A. Kaplan, *Phys. Rev. Lett.* **17**, 913 (1966).
- [8] B. Huang, G. Clark, E. Navarro-Moratalla, D. R. Klein, R. Cheng, K. L. Seyler, D. Zhong, E. Schmidgall, M. A. McGuire, D. H. Cobden, W. Yao, D. Xiao, P. Jarillo-Herrero, and X. Xu, *Nature (London)* **546**, 270 (2017).
- [9] C. Gong, L. Li, Z. Li, H. Ji, A. Stern, Y. Xia, T. Cao, W. Bao, C. Wang, Y. Wang, Z. Q. Qiu, R. J. Cava, S. G. Louie, J. Xia, and X. Zhang, *Nature (London)* **546**, 265 (2017).
- [10] C. M. Wynn, M. A. Girtu, W. B. Brinckerhoff, K.-I. Sugiura, J. S. Miller, and A. J. Epstein, *Chem. Mater.* **9**, 2156 (1997).
- [11] B. D. Cullity and C. D. Graham, *Introduction to Magnetic Materials* (John Wiley & Sons, 2005).
- [12] J. L. Lado and J. Fernández-Rossier, *2D Materials* **4**, 035002 (2017).
- [13] D.-H. Kim, K. Kim, K.-T. Ko, J. Seo, J. S. Kim, T.-H. Jang, Y. Kim, J.-Y. Kim, S.-W. Cheong, and J.-H. Park, *Phys. Rev. Lett.* **122**, 207201 (2019).
- [14] M. A. McGuire, H. Dixit, V. R. Cooper, and B. C. Sales, *Chem. Mater.* **27**, 612 (2015).
- [15] J. G. Rau, E. Kin-Ho Lee, and H.-Y. Kee, *Phys. Rev. Lett.* **112**, 077204 (2014).
- [16] H.-S. Kim, V. Shankar V., A. Catuneanu, and H.-Y. Kee, *Phys. Rev. B* **91**, 241110(R) (2015).
- [17] P. Peter Stavropoulos, D. Pereira, and H.-Y. Kee, *Phys. Rev. Lett.* **123**, 037203 (2019).
- [18] I. Lee, F. G. Utermohlen, D. Weber, K. Hwang, C. Zhang, J. v. Tol, J. E. Goldberger, N. Trivedi, and P. C. Hammel, *Phys. Rev. Lett.* **124**, 017201 (2020).
- [19] C. Xu, J. Feng, H. Xiang, and L. Bellaiche, *npj Comp. Mater.* **4**, 57 (2018).
- [20] M. Deb and A. K. Ghosh, *J. Phys.: Condens. Matter* **31**, 345601 (2019).
- [21] D. G. Joshi, *Phys. Rev. B* **98**, 060405(R) (2018).
- [22] P. Lampen-Kelley, S. Rachel, J. Reuther, J.-Q. Yan, A. Banerjee, C. A. Bridges, H. B. Cao, S. E. Nagler, and D. Mandrus, *Phys. Rev. B* **98**, 100403(R) (2018).
- [23] See Supplemental Material at <http://link.aps.org/supplemental/10.1103/PhysRevB.101.134418> for additional data and analysis.
- [24] N. Richter, D. Weber, F. Martin, N. Singh, U. Schwingenschlögl, B. V. Lotsch, and M. Kläui, *Phys. Rev. Mater.* **2**, 024004 (2018).
- [25] J. W. Lynn, R. W. Erwin, J. A. Borchers, Q. Huang, A. Santoro, J.-L. Peng, and Z. Y. Li, *Phys. Rev. Lett.* **76**, 4046 (1996).
- [26] J. A. Fernandez-Baca, P. Dai, H. Y. Hwang, C. Kloc, and S.-W. Cheong, *Phys. Rev. Lett.* **80**, 4012 (1998).
- [27] J. H. E. Griffiths, *Nature (London)* **158**, 670 (1946).
- [28] A. T. Abdalian, B. Briat, C. Dugautier, and P. Moch, *J. Phys. C: Solid State Phys.* **20**, 2465 (1987).
- [29] J. F. Dillon and C. E. Olson, *J. Appl. Phys.* **36**, 1259 (1965).
- [30] W. Jin, H. H. Kim, Z. Ye, S. Li, P. Rezaie, F. Diaz, S. Siddiq, E. Wauer, B. Yang, C. Li, S. Tian, K. Sun, H. Lei, A. W. Tsai, L. Zhao, and R. He, *Nat. Commun.* **9**, 5122 (2018).
- [31] L. Chen, J.-H. Chung, B. Gao, T. Chen, M. B. Stone, A. I. Kolesnikov, Q. Huang, and P. Dai, *Phys. Rev. X* **8**, 041028 (2018).
- [32] Y. Deng, Y. Yu, Y. Song, J. Zhang, N. Z. Wang, Z. Sun, Y. Yi, Y. Z. Wu, S. Wu, J. Zhu, J. Wang, X. H. Chen, and Y. Zhang, *Nature (London)* **563**, 94 (2018).
- [33] Z. Fei, B. Huang, P. Malinowski, W. Wang, T. Song, J. Sanchez, W. Yao, D. Xiao, X. Zhu, A. F. May, W. Wu, D. H. Cobden, J.-H. Chu, and X. Xu, *Nat. Mater.* **17**, 778 (2018).
- [34] M. Bonilla, S. Kolekar, Y. Ma, H. C. Diaz, V. Kalappattil, R. Das, T. Eggers, H. R. Gutierrez, M.-H. Phan, and M. Batzill, *Nat. Nanotechnol.* **13**, 289 (2018).
- [35] D. J. O'Hara, T. Zhu, A. H. Trout, A. S. Ahmed, Y. K. Luo, C. H. Lee, M. R. Brenner, S. Rajan, J. A. Gupta, D. W. McComb, and R. K. Kawakami, *Nano Lett.* **18**, 3125 (2018).
- [36] R. I. Bewley, J. W. Taylor, and S. M. Bennington, *Nucl. Instrum. Methods Phys.* **637**, 128 (2011).
- [37] R. A. Ewings, A. Buts, M. D. Le, J. van Duijn, I. Bustinduy, and T. G. Perring, *Nucl. Instrum. Methods Phys. Res. A* **834**, 132 (2016).
- [38] M. A. McGuire, *Crystal* **7**, 121 (2017).
- [39] H. Maier-Leibnitz Zetrum, *Journal of Large-Scale Research Facilities* **1**, A12 (2015).
- [40] D. H. Yu, R. Mole, T. Noakes, S. Kennedy, and R. Robinson, *J. Phys. Soc. Jpn.* **82**, SA027 (2013).
- [41] G. E. Granroth, A. I. Kolesnikov, T. E. Sherline, J. P. Clancy, K. A. Ross, J. P. C. Ruff, B. D. Gaulin, and S. E. Nagler, *J. Phys. Conf. Ser.* **251**, 012058 (2010).
- [42] B. Winn, U. Filges, V. Ovidiu Garlea, M. Graves-Brook, M. Hagen, C. Jiang, M. Kenzelmann, L. Passell, S. M. Shapiro, X. Tong, and I. Zaliznyak, *EPJ Web Conf.* **83**, 03017 (2015).
- [43] A. R. Wildes, H. M. Rønnow, B. Roessli, M. J. Harris, and K. W. Godfrey, *Phys. Rev. B* **74**, 094422 (2006).
- [44] E. J. Samuels, R. Silberglipt, G. Shirane, and J. P. Remeika, *Phys. Rev. B* **3**, 157 (1971).
- [45] T. J. Williams, A. A. Aczel, M. D. Lumsden, S. E. Nagler, M. B. Stone, J.-Q. Yan, and D. Mandrus, *Phys. Rev. B* **92**, 144404 (2015).
- [46] R. J. Birgeneau, M. Greven, M. A. Kastner, Y. S. Lee, B. O. Wells, Y. Endoh, K. Yamada, and G. Shirane, *Phys. Rev. B* **59**, 13788 (1999).
- [47] G. T. Lin, X. Luo, F. C. Chen, J. Yan, J. J. Gao, Y. Sun, W. Tong, P. Tong, W. J. Lu, Z. G. Sheng, W. H. Song, X. B. Zhu, and Y. P. Sun, *Appl. Phys. Lett.* **112**, 072405 (2018).

- [48] S. Toth and B. Lake, *J. Phys.: Condens. Matter* **27**, 166002 (2015).
- [49] H. W. de Wijn, L. R. Walker, S. Geschwind, and H. J. Guggenheim, *Phys. Rev. B* **8**, 299 (1973).
- [50] F. Demmel and T. Chatterji, *Phys. Rev. B* **76**, 212402 (2007).
- [51] Z. Zhang, J. Shang, C. Jiang, A. Rasmita, W. Gao, and T. Yu, *Nano Lett.* **19**, 3138 (2019).
- [52] L. Chen, B. Gao, J. H. Chung, T. Chen, R. Ewings, and P. Dai, Spin wave excitations in the 2D honeycomb ferromagnets, STFC ISIS Neutron and Muon Source (2018), doi: [10.5286/ISIS.E.RB1820251](https://doi.org/10.5286/ISIS.E.RB1820251).